

COMMUNICATION

View Article Online
View Journal | View IssueCite this: *J. Mater. Chem. A*, 2019, 7, 27241Received 16th September 2019
Accepted 11th November 2019

DOI: 10.1039/c9ta10226d

rsc.li/materials-a

The scaling of the ligand concentration and Soret effect induced phase transition in CsPbBr₃ perovskite quantum dots†Jiagen Li,^a Menglei Hu,^b Zhaojin Wang,^b Yihua Lu,^a Kai Wang^b and Xi Zhu^{*a}

An intelligent chemistry strategy based automated machine is applied for the study of the phase transition in CsPbBr₃ quantum dots (QDs). With an *in situ* photoluminescence (PL) signal detection and analysis module, oleyl amine (OLA) and oleyl acid (OA) ligand concentration dependent diffusion pictures are well derived, a three-stage power-law scaling is disclosed on the ligand concentration dependent growth, and a phase transformation from CsPbBr₃ to Cs₄PbBr₆ QDs is confirmed. Based on the experimental analysis associated with the G0W0–BSE calculation, we confirmed that there is no significant PL signal in the pure Cs₄PbBr₆ structure. With a steady temperature control module, we find that the ligand concentration and the Soret effect are isomorphic for the mass flux in the QD nucleation and phase transformation. We find that the activity of surface states can be essential for the size dependence of the Soret effect in a general way.

Inorganic lead halide perovskite (LHP) materials, like CsPbBr₃ quantum dots (QDs), can be synthesized in narrow size distribution with sharp peak emissions in the RGB range,^{1,2} and they are supposed to be important materials for display applications due to their remarkable fluorescence properties.³ The basic structure of CsPbBr₃ QDs consists of the PbBr₆ octahedron and the Cs⁺ ions, and besides the traditional CsPbBr₃ phase, other derivatives like Cs₄PbBr₆ and CsPb₂Br₅ can also be formed individually^{4–6} or as hybrids with CsPbBr₃,^{7,8} which exhibit various optical properties like photoluminescence.^{9,10} For example, a 1000 times concentration of OA/OLA can induce the CsPbBr₃ to Cs₄PbBr₆ phase transition under ambient conditions at room temperature,⁴ while more PbBr₂ salt could alternatively induce the reversible phase transition between CsPbBr₃ and Cs₄PbBr₆.¹¹ However, the details of phase transitions

among the CsPbBr₃, CsPb₂Br₅ and Cs₄PbBr₆ phases still require extensive research work to disclose concrete information on the phase transition process.

Here in this work, by using an automated intelligent chemistry robotics system, and with precise control of the OA/OLA quantity and other experimental conditions including reaction time and temperature, we comprehensively studied the phase transition from the CsPbBr₃ to Cs₄PbBr₆ crystal structures, and we found that the Soret effect¹² including both the concentration and temperature gradients can be derived from the phase transition.

The synthesis of CsPbBr₃ QDs is carried out in an AIR-Chem system,¹³ and the workflow chart is shown in Fig. 1. The cloud data center connects the human operators and the experimental devices through a PC terminal or mobile device. The robot performed most of the operations including solid sample

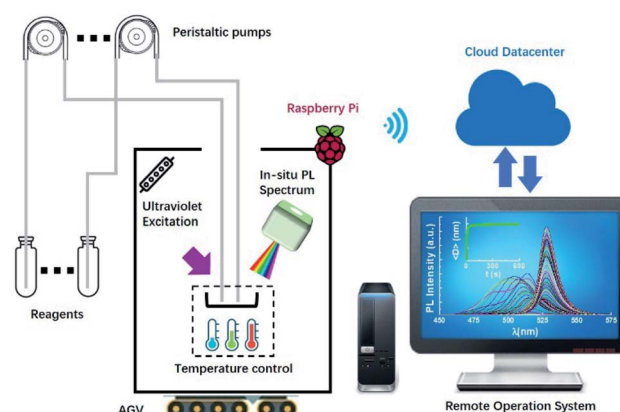


Fig. 1 The automated chemical synthesis system. The solid reactants include PbBr₂ and CsBr, and the liquid reactants include *p*-xylene and DMF, which are prepared using AGV supported robotic modules, remotely controlled by a personal computer (PC) terminal or mobile device through the cloud server. Then the system activates the reaction with the real-time temperature control system and PL system; the analysis data are feedback to the PC terminal or mobile devices for user check.

^aShenzhen Institute of Artificial Intelligence and Robotics for Society (AIRS), Shenzhen, Guangdong, 518129, P. R. China. E-mail: zhuxi@cuhk.edu.cn

^bDepartment of Electrical and Electronic Engineering, Southern University of Science and Technology, Shenzhen, Guangdong, 518055, P. R. China. E-mail: wangk@sustech.edu.cn

† Electronic supplementary information (ESI) available. See DOI: 10.1039/c9ta10226d

(PbBr₂, CsBr, etc.) preparation, and precursor solutions with liquid solvents are injected by a micro-injection system and a semiconductor-based cooling system is integrated into the reaction parts. The automatic guided vehicle (AGV) supports the sample preparation under offsite conditions; the cloud computing technology supports the remote control of

experimental processing by a PC or smartphone. A PL signal analyzing system reads the *in situ* experimental data (for example, PL spectrum and size monitoring from 1 s to 600 s during reprecipitation of CsPbBr₃ QDs, the insert picture on a PC screen at the bottom right of Fig. 1) using a built-in fiber and spectrometer. For the QD system, the PL information is mapped onto the average particle size ($\langle D^{\text{PL}} \rangle$) or $\langle D \rangle$ from a well benchmarked effective mass approximation (EMA).¹⁴ The number of ligands varies from the relative Pb molar ratio from 1.4 to 56.25, which equals the various volumes of OA and OLA in the precursor. Experimental details are in ESI S1.†

Fig. 2(a) shows the (OA + OLA)/Pb molar ratio C_{lig} dependent average radius $\langle D \rangle$ of the CsPbBr₃ QDs. Since the concentration and amount of Pb keep constant in all the experiments and independent of the (OA + OLA) solution, the (OA + OLA)/Pb molar ratio equals the concentration of the OA and OLA ligands C_{lig} . For the perovskite QD system, the PL information can be applied to derive the PL based average QD diameter directly $\langle D \rangle$. Here in this work, the $\langle D \rangle$ values agree well with the experimental data from TEM images (see Fig. 3 for details). The datasets in Fig. 2(a) show a distinct three stage scaling character for $C_{\text{lig}} \propto \langle D \rangle^p$, which can be numerically fitted with power -3 (indicated by a blue solid line) and -1 (indicated by a green solid line) respectively, and the meaning of the power-law index will be discussed in the next part, while the scaling fails for larger $C_{\text{lig}} > 25$ values, as colored in green in Fig. 2(a); $\langle D \rangle$ is a statistical measurement of the size information; the power p can well correlate with the C_{lig} dependent volume and surface change of the QDs. Fig. 2(b) plots the details of growth rate $\langle \dot{D} \rangle$ under various C_{lig} as marked by the ticks. The four datasets in each C_{lig} correspond to the derived experimental data at 0 s, 5 s,

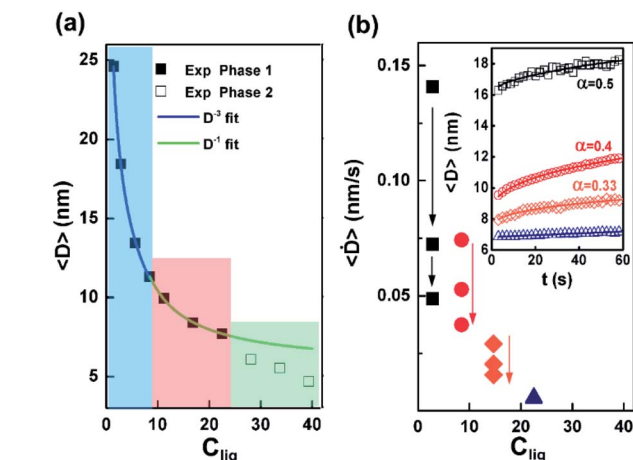


Fig. 2 (a) The (OA + OLA)/Pb molar ratio C_{lig} dependent $\langle D \rangle$ for the QDs. The experimental data are plotted as solid squares (for the CsPbBr₃ phase) and hollow squares (for the Cs₄PbBr₆ phase) respectively. The blue and green lines represent the cube and linear inverse fit. (b) The C_{lig} dependent average growth rate $\langle \dot{D} \rangle$. The inserted figure shows the average $\langle D \rangle$ in the variant C_{lig} condition. The $\langle D \rangle \sim t$ is fitted as a power-law $\langle D \rangle = At^\alpha + D_0$, and the value of α derived from LSW theory can be referred to the diffusion or nucleation dependent event.^{15,16}

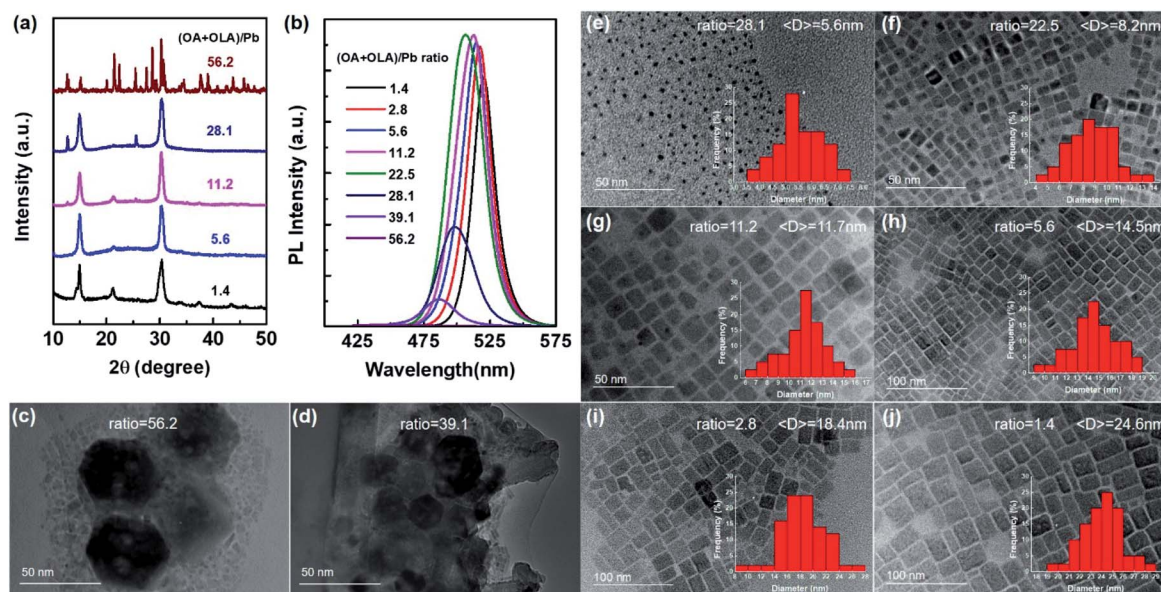


Fig. 3 XRD pattern, PL spectrum and TEM images of LHP nanocrystals synthesized under different C_{lig} . With the increase of C_{lig} , (a) the diffraction peak near 12 degree grows stronger, which indicates the gradual formation of the Cs₄PbBr₆ structure. (b) The blue-shift of the PL center wavelength refers to the decrease of crystal size. Along the phase changing process, the PL intensity decayed rapidly. (c and d) Hexagonal Cs₄PbBr₆ nanocrystal was observed under TEM at high (OA + OLA)/Pb ratios. (e–j) Particle size distribution of CsPbBr₃ nanocrystals was analyzed before the phase transition.

10 s and 15 s after the start of nucleation, as indicated by the arrow direction. We can see that the growth speed $\langle \dot{D} \rangle$ decreases with time in all four datasets. In the small ligand concentration condition, as shown in the inset picture in Fig. 2(b), with the increase of concentration, the QDs grow at the scale of $\langle D \rangle \sim t^{0.50}$ downwards $\langle D \rangle \sim t^{0.33}$, which corresponds to the transition of the typical reaction limited mechanism to the typical diffusion limited mechanism in the classical LSW theory.^{15,16} In the low C_{lig} condition, as shown by the black square dots in Fig. 2(b), the OA/OLA ligands cover a lower QD surface area, and the surface diffusion is more dominant which makes the nucleation reaction limited, with time scaling $\langle D \rangle \sim t^{0.50}$. For the high C_{lig} condition as shown by the orange diamond dots in Fig. 2(b), the high coverage of OA/OLA ligands blocks the mass diffusion channels which turns the nucleation type into diffusion limited with scaling $\langle D \rangle \sim t^{0.33}$, while for the extra high C_{lig} , $\langle \dot{D} \rangle \approx 0$, as shown by the triangle (navy blue) in Fig. 2(b). As reported by previous work, the large OA/OLA concentration (C_{lig}) can directly induce the phase transition,⁴ under which circumstance the PL based $\langle D \rangle$ theory fails. Here based on our experimental data in Fig. 2(a), the concentration-dependent detailed events can be proposed as the two stage C_{lig} dependent $\langle D \rangle$, as shown in Fig. 3. At the start of the reaction, the nucleation events happens extremely quickly in the nano-second (ns) time scale.¹⁷ The ligand density C_{lig} in the solution can be calculated as the product of the nucleus density (n_{QD}) times the coverage of ligand on each QD surface, as defined as D_{cover} , then we have

$$C_{\text{lig}} \propto n_{\text{QD}} \times D_{\text{cover}} \quad (1)$$

Due to the large surface areas of the QDs, usually $D_{\text{cover}} \gg 1$, and due to the repulsion between the ligands¹⁸ on the same surface, usually when C_{lig} is small ($C_{\text{lig}}^{\text{small}}$) the ligand will try to cover more nuclei rather than aggregate on the mono one, then C_{lig} can be expressed as

$$C_{\text{lig}}^{\text{small}} \propto n_{\text{QD}} D_{\text{cover}} = \frac{M_{\text{QD}} D_{\text{cover}}}{\langle M \rangle} = \frac{6 M_{\text{QD}} D_{\text{cover}}}{\pi \langle \rho \rangle \langle D^3 \rangle} \propto \langle D^{-3} \rangle \quad (2)$$

In eqn (2), $\langle \rho \rangle$ is the average mass density of the QDs, which is considered constant here; M_{QD} refers to the total mass of the reactants minus the solubility in the solution, which we assume is only dependent on the temperature. $\langle D^3 \rangle$ is the average radius to the power of 3. Since in the low concentration condition the ligand prefers to cover more nuclei as discussed above, if we assume D_{cover} varies a little in the small ligand concentration condition, we can get the relationship $C_{\text{lig}}^{\text{small}} \propto \langle D^{-3} \rangle$ derived from eqn (2), which can be well identified experimentally as shown in Fig. 2(a)'s blue shadow area.

The conclusion in eqn (2) can be understood as the conservation of M_{QD} , and for the small number of QD nuclei N indexed by a small value of $C_{\text{lig}}^{\text{small}}$, the average mass M_{QD}/N should be large. As shown in the inset picture in Fig. 2(b), with increasing C_{lig} , $\langle D \rangle$ starts to scale with $t^{0.33}$; the growth is of diffusion limited type; the D_{cover} correlates more with the surface flux, and the new pictures become:

$$\begin{aligned} C_{\text{lig}}^{\text{large}} &= n_{\text{QD}} D_{\text{cover}} = n_{\text{QD}} \times A \times J \\ &= \frac{\pi n_{\text{QD}} J \langle D^2 \rangle}{4} \propto \langle D^{-3} \rangle \langle D^2 \rangle \propto \langle D^{-1} \rangle \end{aligned} \quad (3)$$

Here in eqn (3), J is the bonding density of the Pb-ligand, A is the total surface area and $\langle D^2 \rangle$ is the average radius to the power of 2. n_{QD} is proportional to $\langle D^{-3} \rangle$ as shown in eqn (3). J is only dependent on coordination chemistry. From eqn (3), we can get the relationship $C_{\text{lig}} \propto \langle D^{-1} \rangle$ derived from the large concentration of ligand as expressed in eqn (3), which agrees well with the experimental data in Fig. 2(a)'s light red area. Fig. 3 shows the detailed scheme of the two-stage scaling. However, when n_{QD} and D_{cover} are large enough and C_{lig} still keeps increasing, the $\langle D^{-1} \rangle$ scaling starts to disagree with the experimental data, as shown in Fig. 2(a)'s green areas, and there is no distinct particle growth information based on the PL methodology, as shown in Fig. 2(b)'s triangle (navy blue) plot. There could be some structural phase changing events.¹⁹ The XRD patterns (Fig. 3(a)) and the hexagonal crystal shape (Fig. 3(c) and (d)) of samples prepared under various C_{lig} gave strong evidence of this CsPbBr_3 to Cs_4PbBr_6 phase changing process. Additionally, the decay trends of PL (Fig. 3(b)) agreed well with the recent work of Alivisatos *et al.*,⁴ which proved the reproducibility of this method. Particle size analysis based on TEM images of LHP (Fig. 3(e)–(j)) was applied to check the precision of the size mapping from $\langle D^{\text{PL}} \rangle$ to $\langle D \rangle$. A sub-nanometer resolution was verified by comparing the size information in Fig. 2(a).

The above discussion about the colorless phase is solely induced by the concentration of ligand concentration C_{lig} ; moreover, through the temperature control module, we find that the temperature gradient dependence can reproduce color transitions as well. As shown in Fig. 4(a), starting from the green orthorhombic CsPbBr_3 phase, by applying negative temperature gradients, the solution will turn colorless when the solvent

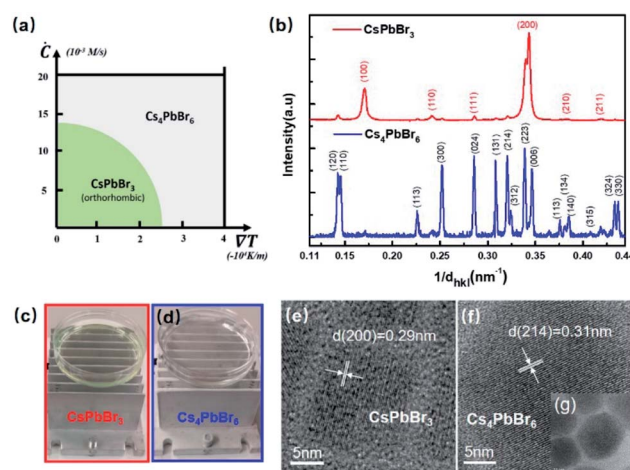


Fig. 4 (a) The schematic relationship between the temperature gradient and concentration gradient for the phase diagram. (b) The XRD patterns of the CsPbBr_3 and Cs_4PbBr_6 at room temperature in this work. Temperature gradient dependence of the transformation from (c) CsPbBr_3 (light green) to (d) Cs_4PbBr_6 (colorless). The HR-TEM images of (e) CsPbBr_3 QDs and (f and g) Cs_4PbBr_6 QDs samples.

(*para*-xylene) is frozen, while the colorless state can still be retained even after the temperature is recovered to room temperature. These temperature gradient induced phase changes are typical of the Soret effect, which indicates that the concentration and temperature gradient can co-influence the particle flux, as^{12,20}

$$J = -D \frac{dc}{dt} - \kappa \frac{dT}{dx} \quad (4)$$

where J is the flux, c is the solute concentration in the solution, T is the temperature, D and κ are coefficients, and t and x are time and space. Eqn (4) indicates that the particle current J is dependent on both the mass concentration gradient and the temperature gradient with length; in other words, the time gradient of c (\dot{c}) is analogous to the space size gradient of temperature (∇T), which means that the ligand concentration and the Soret effect are isomorphic for the mass flux. Fig. 4(a) shows the scheme of the phase diagram of the phase transition between the green (CsPbBr₃) and colorless (Cs₄PbBr₆) phases (see Fig. 4(c) and (d)). \dot{c} here is determined by c and the average growth time of QDs. ∇T was calculated by dividing temperature variance with the distance between two surfaces.

The Ludwig–Soret adequately describes a temperature gradient induced thermophoretic driving force, which can separate distinct material phases.^{21–23} It is a complicated phenomenon associated with both the temperature dependence of the entropy change in statistics and the atomic bonding or molecular interaction changes in chemistry.²⁴ There is still a debate whether it is dependent on the particle size²⁵ or not.²⁴ Our experimental data show that the phase transition from CsPbBr₃ to Cs₄PbBr₆ occurs more quickly when n_{QD} increases, in which condition the system has a smaller $\langle D \rangle$ and larger surface area. These results are more close to the size dependent understanding in which the Soret coefficient is proportional to the surface area.^{25,26} Something in common for the size-dependent Soret effect is that the materials chosen for the study have active surface chemical bonding states, like the perovskite QD system studied in this work, and the surface state is more active due to the dangling bonds and the hydrogen bonds like those in the molecular system in the literature.²⁵ The size-dependent Soret effect in micro-emulsion droplets has been investigated in inertial water–oil interface states.²⁴

Based on this work, we propose that the surface states can affect the size dependence of the Soret effect. To obtain structure information, the crystal structure of CsPbBr₃ will be transformed from the orthorhombic to the cubic phase *via* a tetragonal phase by increasing the temperature to 130 °C (ref. 27) (Table S1†). To investigate the crystalline structure of the colorless sample, we performed XRD with a copper K- α wavelength of 1.54 Å. Shown in Fig. 4(b), Cs₄PbBr₆ structure was identified according to the reference XRD pattern JCPDS No. 73-2478. High-resolution transmission electron microscopy (HR-TEM) showed that the individual nanocrystal lattice structures belong to orthorhombic CsPbBr₃ and hexagonal Cs₄PbBr₆ in Fig. 4(e) and (f). With the measurement of the inter-planar distance of the two lattices, the results reveal that the inter-

planar distance of orthorhombic CsPbBr₃ is 0.29 nm that can be assigned to the (200) plane, and the inter-planar distance of Cs₄PbBr₆ is 0.31 nm that can be indexed to the (214) plane which is in contrast to the XRD patterns. What's more, the crystal structure of Cs₄PbBr₆ can be further confirmed through XRD Rietveld refinement²⁸ to be the hexagonal phase with a space group of $R\bar{3}c$ and lattice parameters 13.7 Å, 13.7 Å, and 17.3 Å.

There is still a debate about the origin of the PL signal in the Cs₄PbBr₆ or Cs₄PbBr₆ phases.^{4,29–32} In the literature some defects of CsPbBr₃ can coexist in the CsPbBr₃/Cs₄PbBr₆ hybrid structure, which makes the origin of the PL technically more diverse.^{30,31,33} Different from the mixture of CsPbBr₃ and Cs₄PbBr₆ phases obtained from the chemical type experimental strategy, like additive ligands,^{11,18} the XRD patterns in Fig. 4(b) show a defect-free crystal, and our experimental data support that there is no PL signal in the Cs₄PbBr₆ crystal. However, ∇T here should be ensured to have a large value by controlling the thickness of QD solutions, and an extensive volume of QD solution will reduce ∇T , causing an incomplete phase transition. The incomplete transition induced middle state can be well observed from the XRD patterns as shown in Fig. S1.† We collected the PL spectra (Fig. 5(a)) of CsPbBr₃ and middle state samples. The PL of the green CsPbBr₃ sample exhibits one strong emission peak at 509 nm and a full width at half maximum (FWHM) of 16.3 nm, while applying the temperature gradient $\nabla T = 3 \times 10^4 \text{ K m}^{-1}$, with temperature changing $\Delta T = -30 \text{ K}$ (from room temperature to 260 K), the green luminescence gradually changes to colorless (99% reduction of the PL intensity from 1861 to 45 in arbitrary units), as shown in Fig. 5(a). The ∇T value agrees well with the simulation data (Fig. 5(b) and (c)) under the same cooling area size. Compared with pure Cs₄PbBr₆ samples (totally no PL signal in the visible light region), the weak PL intensity is attributed to the hybridized CsPbBr₃ composition. Further, our simulation data with G0W0 band structure calculations (see the Simulation methods section) as shown in Fig. 5(d) indicate that the band gap of the orthorhombic Cs₄PbBr₆ phase is about 6.0 eV, which is larger than the PBE0 data (3.88 eV)³⁴ and the BSE absorption peak lies at around 5.8 eV; taking into account a 100 meV Stokes shift value in the CsPbBr₃ system,³⁵ the emission peak can be around 5.7 eV, far from the energy range of visible light. The ultra-short PL lifetime (<0.3 ns) from middle state samples, which is much shorter than that from CsPbBr₃ nanocrystals, indicates a defect-induced picture of PL from the 113/416 hybrid structure (Fig. 5(e), Table S2 in ESI S2†). Our experimental and simulation data suggest that the pure Cs₄PbBr₆ sample is colorless and shows no PL effect. In addition, we applied this fast cooling method to CsPb(Br₁I₂) nanocrystals, and hybrid phases of CsPb(Br₁I₂) and Cs₄Pb(Br₂I₄) were obtained (XRD patterns are shown in Fig. S2†) to verify the universality of this Ludwig–Soret effect in the phase transition of CsPbX₃ and Cs₄PbX₆ nanocrystals.

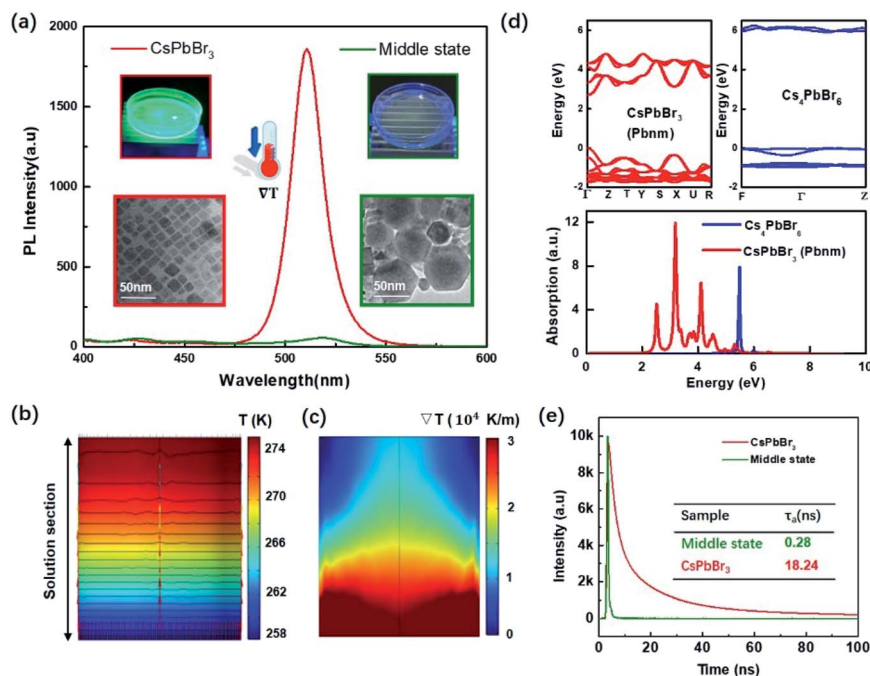


Fig. 5 (a) PL spectra of CsPbBr₃ and middle state (CsPbBr₃/Cs₄PbBr₆ hybrid structure) samples with $\lambda_{\text{ex}} = 365$ nm. Insert picture shows the photograph and TEM images of the two samples. (b and c) The temperature (T) and temperature gradient (∇T) of the center section in *p*-xylene solution, simulated with *COMSOL Multiphysics*. Arrows represent the direction and strength (indicated by colors) of ∇T . (d) G0W0 band structures and simulated BSE absorption spectra of the CsPbBr₃ and Cs₄PbBr₆ crystals. (e) Time-resolved PL decays of CsPbBr₃ and middle state LHP samples with $\lambda_{\text{ex}} = 360$ nm.

Conclusions

To conclude, for the CsPbBr₃ perovskite QD system, we systematically studied the ligand concentration (C_{lig}) dependent scaling with the nucleation and growth events. A three-stage picture for monomer nucleation, particle growth and phase transition was directly derived from the *in situ* PL defined band gap (D). A colorless Cs₄PbBr₆ was transformed in the high C_{lig} condition. Due to the active surface chemical bonding states in the perovskite QDs, the Cs₄PbBr₆ phase can also be synthesized through the Ludwig-Soret effect, *i.e.*, the temperature gradient as well.

Simulation methods

To calculate the G0W0 band structure for the CsPbBr₃ and Cs₄PbBr₆ crystal structures, we first get the wavefunction of the ground state by using the Perdew–Burke–Ernzerhof (PBE)³⁶ exchange–correlation functional in Abinit code.³⁷ A 60 Ry kinetic energy cut-off and $8 \times 8 \times 8$ K-sampling are applied for the ground state calculation. For the G0W0 quasi-particle corrections, the screening effect is dealt with the plasmon-pole approximation.³⁸ The electron-hole interactions for the many-body Green function are solved using the Bethe–Salpeter equation.³⁹

Conflicts of interest

There are no conflicts to declare.

Acknowledgements

This work is supported by the Shenzhen Fundamental Research Foundation (JCYJ20170818103918295), the National Natural Science Foundation of China (Grant No. 21805234 and 61875082) and the National Key Research and Development Program (No. 2017YFE0120400). Funding from the Shenzhen Institute of Artificial Intelligence and Robotics for Society (AIRS) is appreciated.

References

- M. A. Becker, R. Vaxenburg, G. Nedelcu, P. C. Sercel, A. Shabaev, M. J. Mehl, J. G. Michopoulos, S. G. Lambrakos, N. Bernstein, J. L. Lyons, T. Stöferle, R. F. Mahrt, M. V. Kovalenko, D. J. Norris, G. Rainò and A. L. Efros, *Nature*, 2018, **553**, 189.
- Q. A. Akkerman, G. Rainò, M. V. Kovalenko and L. Manna, *Nat. Mater.*, 2018, **17**, 394–405.
- M. V. Kovalenko, L. Protesescu and M. I. Bodnarchuk, *Science*, 2017, **358**, 745–750.
- Z. Liu, Y. Bekenstein, X. Ye, S. C. Nguyen, J. Swabeck, D. Zhang, S.-T. Lee, P. Yang, W. Ma and A. P. Alivisatos, *J. Am. Chem. Soc.*, 2017, **139**, 5309–5312.
- I. Dursun, M. De Bastiani, B. Turedi, B. Alamer, A. Shkurenko, J. Yin, A. M. El-Zohry, I. Gereige, A. AlSaggaf, O. F. Mohammed, M. Eddaoudi and O. M. Bakr, *ChemSusChem*, 2017, **10**, 3746–3749.

- 6 F. Palazon, S. Dogan, S. Marras, F. Locardi, I. Nelli, P. Rastogi, M. Ferretti, M. Prato, R. Krahne and L. Manna, *J. Phys. Chem. C*, 2017, **121**, 11956–11961.
- 7 C. de Weerd, J. Lin, L. Gomez, Y. Fujiwara, K. Suenaga and T. Gregorkiewicz, *J. Phys. Chem. C*, 2017, **121**, 19490–19496.
- 8 X. Zhang, Z. Jin, J. Zhang, D. Bai, H. Bian, K. Wang, J. Sun, Q. Wang and S. F. Liu, *ACS Appl. Mater. Interfaces*, 2018, **10**, 7145–7154.
- 9 M. De Bastiani, I. Dursun, Y. Zhang, B. A. Alshankiti, X.-H. Miao, J. Yin, E. Yengel, E. Alarousu, B. Turedi, J. M. Almutlaq, M. I. Saidaminov, S. Mitra, I. Gereige, A. AlSaggaf, Y. Zhu, Y. Han, I. S. Roqan, J.-L. Bredas, O. F. Mohammed and O. M. Bakr, *Chem. Mater.*, 2017, **29**, 7108–7113.
- 10 J. Yin, P. Maity, M. De Bastiani, I. Dursun, O. M. Bakr, J.-L. Brédas and O. F. Mohammed, *Sci. Adv.*, 2017, **3**, e1701793.
- 11 G. Long, C. Jiang, R. Sabatini, Z. Yang, M. Wei, L. N. Quan, Q. Liang, A. Rasmita, M. Askerka, G. Walters, X. Gong, J. Xing, X. Wen, R. Quintero-Bermudez, H. Yuan, G. Xing, X. R. Wang, D. Song, O. Voznyy, M. Zhang, S. Hoogland, W. Gao, Q. Xiong and E. H. Sargent, *Nat. Photonics*, 2018, **12**, 528–533.
- 12 C. Ludwig, *Sitz. ber. Math.-Naturw. Clas. Kais. Akad. Wiss.*, 1856, **20**, 539.
- 13 J. Li, Y. Lu, Y. Xu, C. Liu, Y. Tu, S. Ye, H. Liu, Y. Xie, H. Qian and X. Zhu, *J. Phys. Chem. A*, 2018, **122**, 9142–9148.
- 14 G. Dresselhaus, *J. Phys. Chem. Solids*, 1956, **1**, 14–22.
- 15 C. Wagner, *Z. Elektrochem.*, 1961, **65**, 581–591.
- 16 I. M. Lifshitz and V. V. Slyozov, *J. Phys. Chem. Solids*, 1961, **19**, 35–50.
- 17 G. C. Sossio, J. Chen, S. J. Cox, M. Fitzner, P. Pedevilla, A. Zen and A. Michaelides, *Chem. Rev.*, 2016, **116**, 7078–7116.
- 18 N. Pradhan, D. Reifsnnyder, R. Xie, J. Aldana and X. Peng, *J. Am. Chem. Soc.*, 2007, **129**, 9500–9509.
- 19 D. Li, G. Wang, H.-C. Cheng, C.-Y. Chen, H. Wu, Y. Liu, Y. Huang and X. Duan, *Nat. Commun.*, 2016, **7**, 11330.
- 20 R. J. Asaro, D. Farkas and Y. Kulkarni, *Acta Mater.*, 2008, **56**, 1243–1256.
- 21 L. Lin, J. Zhang, X. Peng, Z. Wu, A. C. H. Coughlan, Z. Mao, M. A. Bevan and Y. Zheng, *Sci. Adv.*, 2017, **3**, e1700458.
- 22 S. B. Kukadiya, P. K. Chan and M. Mehrvar, *Macromol. Theory Simul.*, 2009, **18**, 97–107.
- 23 J. Chipman, *J. Am. Chem. Soc.*, 1926, **48**, 2577–2589.
- 24 D. Vigolo, G. Brambilla and R. Piazza, *Phys. Rev. E: Stat., Nonlinear, Soft Matter Phys.*, 2007, **75**, 040401.
- 25 S. Duhr and D. Braun, *Proc. Natl. Acad. Sci. U. S. A.*, 2006, **103**, 19678–19682.
- 26 R. D. Astumian, *Proc. Natl. Acad. Sci. U. S. A.*, 2007, **104**, 3–4.
- 27 S. Hirotsu, J. Harada, M. Iizumi and K. Gesi, *J. Phys. Soc. Jpn.*, 1974, **37**, 1393–1398.
- 28 J. Rodríguez-Carvajal, *Phys. B*, 1993, **192**, 55–69.
- 29 M. I. Saidaminov, J. Almutlaq, S. Sarmah, I. Dursun, A. A. Zhumeckenov, R. Begum, J. Pan, N. Cho, O. F. Mohammed and O. M. Bakr, *ACS Energy Lett.*, 2016, **1**, 840–845.
- 30 Y. Zhang, M. I. Saidaminov, I. Dursun, H. Yang, B. Murali, E. Alarousu, E. Yengel, B. A. Alshankiti, O. M. Bakr and O. F. Mohammed, *J. Phys. Chem. Lett.*, 2017, **8**, 961–965.
- 31 Y. Wang, D. Yu, Z. Wang, X. Li, X. Chen, V. Nalla, H. Zeng and H. Sun, *Small*, 2017, **13**, 1701587.
- 32 N. Riesen, M. Lockrey, K. Badek and H. Riesen, *Nanoscale*, 2019, **11**, 3925–3932.
- 33 Q. A. Akkerman, S. Park, E. Radicchi, F. Nunzi, E. Mosconi, F. De Angelis, R. Brescia, P. Rastogi, M. Prato and L. Manna, *Nano Lett.*, 2017, **17**, 1924–1930.
- 34 J. Yin, P. Maity, M. De Bastiani, I. Dursun, O. M. Bakr, J.-L. Brédas and O. F. Mohammed, *Sci. Adv.*, 2017, **3**, e1701793.
- 35 M. C. Brennan, J. Zinna and M. Kuno, *ACS Energy Lett.*, 2017, **2**, 1487–1488.
- 36 J. P. Perdew, K. Burke and M. Ernzerhof, *Phys. Rev. Lett.*, 1996, **77**, 3865–3868.
- 37 X. Gonze, B. Amadon, P. M. Anglade, J. M. Beuken, F. Bottin, P. Boulanger, F. Bruneval, D. Caliste, R. Caracas, M. Côté, T. Deutsch, L. Genovese, P. Ghosez, M. Giantomassi, S. Goedecker, D. R. Hamann, P. Hermet, F. Jollet, G. Jomard, S. Leroux, M. Mancini, S. Mazevet, M. J. T. Oliveira, G. Onida, Y. Pouillon, T. Rangel, G. M. Rignanese, D. Sangalli, R. Shaltaf, M. Torrent, M. J. Verstraete, G. Zerah and J. W. Zwanziger, *Comput. Phys. Commun.*, 2009, **180**, 2582–2615.
- 38 R. W. Godby and R. J. Needs, *Phys. Rev. Lett.*, 1989, **62**, 1169–1172.
- 39 M. S. Hybertsen and S. G. Louie, *Phys. Rev. B: Condens. Matter Mater. Phys.*, 1986, **34**, 5390–5413.